Theoretical and experimental investigation on structural, electronic and magnetic properties of layered Mn_5O_8†

M. R. Ashwin Kishore,[a] H. Okamoto,[b] Lokanath Patra,[a] R. Vidya,[c] Anja O. Sjåstad,[b] H. Fjellvåg[b] and P. Ravindran*[ab]

We have investigated the crystal, electronic, and magnetic structures of Mn_5O_8 by means of state-of-the-art density functional theory calculations and neutron powder diffraction (NPD) measurements. This compound stabilizes in the monoclinic structure with space group $C2/m$ where the Mn ions are in the distorted octahedral and trigonal prismatic coordinations with oxygen atoms. The calculated structural parameters based on total energy calculations are found to be in excellent agreement with low temperature NPD measurements when we accounted for the correct magnetic structure and Coulomb correlation effect in the computation. Using fully relativistic generalized-gradient approximation with Hubbard U (GGA+U) we found that the magnetic ordering in Mn_5O_8 is A-type antiferromagnetic and the direction of the easy axis is [1 0 0] in agreement with susceptibility and NPD measurements. However, the calculation without the inclusion of Hubbard U leads to ferrimagnetic half metal as a ground state contradictory to experimental findings, indicating the presence of a strong Coulomb correlation effect in this material. The GGA calculation without the Coulomb correction effect itself is sufficient to reproduce the experimentally observed magnetic moments in various Mn sites. We found that Mn in this material exhibits mixed valence behavior with 2+ and 4+ oxidation states reflecting different magnetic moments in the Mn sites. We explored the electronic band characteristics using total, site-, and orbital-projected density of states which emphasized the mixed-valent nature of Mn. A dominant Mn 3d character of the density of states at Fermi energy is the origin for the metallic behavior of Mn_5O_8. The bond strength analysis based on the crystal orbital Hamiltonian population between constituents indicates strong anisotropy in the bonding behavior which results from the layered nature of its crystal structure. Our bonding analysis shows that there is a noticeable covalent bond between Mn 3d–O 2p states which stabilizes the observed low symmetric structure. Our experimental findings and theoretical predictions suggest that Mn_5O_8 can be classified as a strongly correlated mixed valent antiferromagnetic metal.

1 Introduction

Manganese (Mn) oxides can be considered as an interesting class of materials among various transition metal oxides because they crystallize in different structures with many oxidation states (2+, 3+, and 4+ *etc.*)[1–4] that exhibit exotic magnetic behaviors. Among them, Mn^{2+} has basically no preference on coordination due to the $3d^5$ electronic configuration and it occupies almost indifferently crystallographic sites with coordination numbers of 4, 6, and/or 8, depending on other structural constraints. On the other hand, Mn^{3+} and Mn^{4+} are commonly found in octahedral sites in complex oxides. Also, the Mn^{3+} ($t_{2g}^3 e_g^1$) ion in $LaMnO_3$[5] makes it a typical Jahn–Teller system which results in a distortion of the MnO_6 octahedron with four shorter equatorial bonds and two longer axial bonds. In terms of ionic radius, the difference in the ionic radii between Mn^{2+} and Mn^{3+} [0.185 Å (=0.83–0.645 Å)] is larger than that between Mn^{3+} and Mn^{4+} [0.115 Å (=0.645–0.53 Å, based on $r(O^{2-})$ = 1.40 Å)].[6] Namely, the divalent Mn ion has somehow a unique feature in the oxide form, and this has important consequences on the crystal chemistry and physical properties. Binary manganese oxides such as MnO, Mn_3O_4, Mn_2O_3, MnO_2, and Mn_5O_8 possess a wide variety of technological applications due to their unique structural and physical properties. Owing to the presence of mixed valences of Mn atoms, this family of compounds is a

[a] *Department of Physics, Central University of Tamil Nadu, Thiruvarur, Tamil Nadu, 610101, India. E-mail: raviphy@cutn.ac.in*

[b] *Center for Materials Science and Nanotechnology and Department of Chemistry, University of Oslo, Box 1033 Blindern, N-0315 Oslo, Norway*

[c] *Department of Medical Physics, Anna University, Chennai, 600025, India*

This journal is © the Owner Societies 2016

Phys. Chem. Chem. Phys., 2016, **18**, 27885–27896 | 27885

quite attractive and potential candidate for catalysis, electrode materials for batteries and soft magnetic materials for transformer cores.[7,8] Due to the complex interplay between orbital, spin, and lattice degrees of freedom, Mn oxides exhibit intriguing properties such as colossal magnetoresistance, metal–insulator transitions, charge as well as orbital ordering,[9,10] and complex magnetic behavior.[4,11–14] For example, MnO is a type-II antiferromagnetic (AFM-II) insulator below the Néel temperature of T_N = 118 K,[15] Mn_3O_4 shows a ferrimagnetic (FiM) behavior at T_C = 42 K, upon further cooling it exhibits a spiral spin structure at 39 K and then it transforms into a canted spin array at 33 K.[16–18] α-Mn_2O_3 exhibits a complex noncollinear AFM ordering and β-MnO_2 has a screw-type magnetic structure with ordered helical moments.[19,20] Among the stable binary Mn oxides, Mn_5O_8 has been reported in the literature as a metastable phase.[21–23]

It is reported that the crystal structure of Mn_5O_8 is also isostructural with $Ca_2Mn_3O_8$[24] and $Cu_2Mn_3O_8$.[25] Yamamoto et al.[26] reported that Mn_5O_8 orders antiferromagnetically at Néel temperature $T_N \simeq$ 136 K, which was the highest among most of the known manganese oxides. Mn_5O_8 has higher magnetic transition temperature than its isomorphous compounds such as $Cd_2Mn_3O_8$ ($T_N \simeq$ 10 K) and $Ca_2Mn_3O_8$ ($T_N \simeq$ 60 K) due to the fact that both the interlayer and intralayer distances between magnetic ions in $Cd_2Mn_3O_8$ and $Ca_2Mn_3O_8$ are larger than those in Mn_5O_8 and this will reduce the corresponding exchange integrals in $Cd_2Mn_3O_8$ and $Ca_2Mn_3O_8$, resulting in lower values of Θ and magnetic ordering temperature. In other words, the substitution of nonmagnetic Cd^{2+} and Ca^{2+} ions for the magnetic Mn^{2+} ions weakens the magnetic exchange interactions, which leads to a decrease in the magnetic ordering temperature.

Several other experimental studies also reported that Mn_5O_8 is an antiferromagnet with Néel temperature $T_N \simeq$ 128 K,[27] $T_N \simeq$ 133 K,[28] $T_N \simeq$ 131 K,[29] and $T_N \simeq$ 126 K.[30] A noticeable difference in the reported Néel temperature is due to the finite-size effect on the antiferromagnetic transition temperature T_N.[31,32] In addition to the characteristic antiferromagnetic ordering peak of Mn_5O_8, a sharp peak is observed at around 40 K[27,28] by magnetization measurements which is believed to be associated with T_C of ferrimagnetic Mn_3O_4 because Mn_5O_8 is synthesized by the oxidation of Mn_3O_4. However, our low temperature Neutron Powder Diffraction (NPD) measurements were unable to detect any secondary phases and the details will be discussed below.

X-ray photoemission spectroscopy (XPS) measurements on Mn_5O_8 have been made and the analysis[28,30] confirms the two possible types of Mn with oxidation states 4+ and 2+. It may be noted that it is difficult to distinguish between Mn^{2+} and Mn^{4+} due to the small binding energy shift (less than ca. 1.0 eV) and it will be even more complicated if the Mn is present in mixed valence states.[33] Jeong et al.[34] reported that the Mn^{3+} ions are involved in the oxygen evolution reaction process of Mn_5O_8 nanoparticles, which is contradictory to the XPS analysis mentioned above. Therefore, apart from calculating the Bond Valence Sum (BVS), we have used various theoretical tools to analyze the oxidation of manganese ions in Mn_5O_8 as we have reported earlier.[35]

The details of magnetic ordering, the direction of easy axis, and anisotropy in the magnetic and transport properties for Mn_5O_8 are not yet identified though nanorods of Mn_5O_8 have been reported recently.[28] To our knowledge, no theoretical study on Mn_5O_8 has been reported in the literature. In the present study, we attempt to identify the ground state magnetic structure, electronic structure, and the mixed valent behavior of manganese ions in Mn_5O_8 using experimental measurements and computational studies.

2 Methods

2.1 Experimental details

A polycrystalline sample of Mn_5O_8 was synthesized by a wet chemical reaction route.[36] Prior to NPD measurements, the synthesized sample was characterized by X-ray diffraction and found not to contain detectable impurities. NPD data at 298 K, 70 K, and 9 K were collected with the PUS two-axis diffractometer at the JEEP II reactor, Kjeller, Norway.[37] The powder sample was kept in cylindrical sample holders. Monochromatized neutrons of wavelength 1.5556 Å were obtained by reflection from Ge(311). NPD data were measured in the $10.00° \leq 2\theta \leq 129.95°$ range with a scan-step of $0.05°$. The simulation and Rietveld methods[38] were performed with the Fullprof code.[39] NPD data and reflections from the Displex cryostat at $46.00° \leq 2\theta \leq 46.90°$, $76.90° \leq 2\theta \leq 77.60°$, and $115.90° \leq 2\theta \leq 117.20°$ in all collected NPD data were excluded prior to the refinements. Scale factor, zero point, pseudo-Voigt profile parameters, unit-cell dimensions, positional parameters, together with four isotropic displacement factors, and the magnetic moments of manganese, were entered into the final least-squares refinement.

2.2 Computational details for the full-potential linear augmented plane-wave (FP-LAPW) calculations

Calculations were performed using the standard full-potential linear augmented plane-wave method based on density functional theory (DFT) as implemented in the Wien2k code.[40] We have used the generalized gradient approximation (GGA) of Perdew–Burke–Ernzerhof for the exchange–correlation functional.[41] The muffin tin sphere radii (R_{MT}) values for Mn and O atom were taken to be 1.87 and 1.61 a.u, respectively. The plane wave cut-off parameters were decided by $R_{MT}^{min}K_{max}$ = 7 (the product of the smallest of the atomic sphere radii R_{MT} and the plane wave cut-off parameter K_{max}) and 400 k-points were used over the irreducible part of the first Brillouin zone (IBZ). We have also included both Mott–Hubbard parameter U, and spin–orbit coupling (SO) in the calculations to account for the correlation effect (GGA+U) and the relativistic effect (GGA+SO) respectively. The value of U_{eff} = $U - J$ (U and J are on-site Coulomb and exchange interaction, respectively) chosen for this calculation is 5 eV which is normally used for manganese oxides to account for Coulomb correlation effects. There are many different implementations to calculate the U value precisely.[42–46] Though U is a computational parameter, the calculated magnetic moments, magnetic ground state, etc., for the chosen U value are

27886 | Phys. Chem. Chem. Phys., 2016, **18**, 27885–27896

This journal is © the Owner Societies 2016

in good agreement with the experimental results indicating that the value of the currently used U parameter is justified.

2.3 Computational details for Vienna *ab initio* simulation package (VASP) calculations

Structural optimizations were done using VASP code[47] within the projector augmented wave (PAW) method. The generalized gradient approximation proposed by Perdew, Burke and Ernzrhof (GGA-PBE)[41] was used for the exchange and correlation functional. As we have found earlier that a sufficiently large basis set with a reasonable number of k-points is needed to predict reliable structural parameters for transition metal oxides,[48] we have used the energy cut off of 875 eV and the k-points value is $2 \times 4 \times 4$ for the irreducible part of the first Brillouin zone of base centered monoclinic lattice. The force minimization steps were continued until the maximum Hellmann–Feynman forces acting on each atom was less than 0.01 eV Å^{-1}. Also, the pressure in the unit cell was kept below 1 kbar.

3 Results and discussion

3.1 Crystal structure

Mn_5O_8 possess a layered Birnessite-type structure.[49] The crystal structure reported by Oswald *et al.*[50] for Mn_5O_8 having the compositional formula $Mn_2^{2+}Mn_3^{4+}O_8$ is isotypic with base-centered monoclinic $Cd_2Mn_3O_8$ with space group $C2/m$. This structure can be considered as a layered structure with two formula units per unit cell as indicated in Fig. 1. The overall crystal structure of Mn_5O_8 can be described as infinite sheets of $[Mn_3^{4+}O_8]^{4-}$ where the Mn^{4+} ions are held together by Mn^{2+} ions. This structure consists of distorted MnO_6 ($Mn1O_6^o$ and $Mn2O_6^o$) edge shared octahedral layers with Mn^{4+} ions in the bc plane separated by Mn^{2+} ions as shown in Fig. 1. One fourth of the cationic sites in the main octahedra sheets are vacancies which result in charge imbalance and consequently its composition becomes $[Mn_3^{4+}O_8]^{4-}$. This charge imbalance was neutralized by the Mn^{2+} ions situated above and below the empty Mn^{4+} sites completing the composition $Mn_2^{2+}Mn_3^{4+}O_8$.

Also, the oxygen ions are located in three different sites in Mn_5O_8. One of the $Mn^{4+}(Mn1^o)$ ions is in the $2c$ site (C_{2h} symmetry) coordinated octahedrally to four equatorial O atoms at 1.921 Å and two apical O atoms at 1.937 Å where

the average Mn–O distance is 1.926 Å. The O–Mn–O angles within this $Mn1O_6^o$ octahedron vary between 85° and 95° when O atoms are *cis*-arranged and 180° when O atoms are *trans*-arranged. Two Mn^{4+} ($Mn2^o$) atoms are in $4g$ sites (C_2 symmetry) coordinated by highly distorted octahedra of O atoms with two Mn–O distances at 1.867 Å and two at 1.913 Å and two at 1.971 Å with an average Mn–O distance of 1.917 Å. The O–Mn–O angles within this $Mn2O_6^o$ distorted octahedron vary between 81.9° and 96.4° when the O atoms are *cis*-arranged and between 168.7° and 177.6° when the O atoms are *trans*-arranged. Mn^{2+} ions ($Mn3^t$) form a trigonal-prismatic coordination with six oxygen atoms, out of which three are from one octahedral layer and three are from the next octahedral layer. As shown in Fig. 1, O(1) is coordinated by two Mn^{4+} and two Mn^{2+} ions, O(2) is coordinated by three Mn^{4+} and one Mn^{2+} ions, and O(3) is coordinated by two Mn^{4+} and one Mn^{2+} ion. Due to this difference in coordination of Mn with O atoms, different magnetic moments in various manganese sites arise.

3.2 Magnetic structure

Before discussing the magnetic structure of Mn_5O_8, the NPD data at 298 K based on the result of Rietveld analysis as shown in Fig. 2 is described. Careful indexing of all observed peaks in the collected data confirms the previously proposed systematic extinction scheme,[51] corresponding to the space group of $C2/m$ (No. 12) ($a = 10.372$ Å, $b = 5.733$ Å, $c = 4.860$ Å, and $\beta = 109.4°$). The present NPD pattern at 9 K shows extra intensity compared to that at 298 K, which can be expected from the magnetic reflection arising from magnetic ordering occurring around $T_N = 136$ K as shown in Fig. 3. In order to get more clarity on the magnetic reflections, in Fig. 3 we have also plotted the differential intensity between 298 K and 9 K [$I(9$ K$)–I(298$ K$)$]. We have assumed four possible AFM models in the $1 \times 1 \times 1$ crystal structural dimension, which are shown in Fig. 4 together with the corresponding simulated scattering patterns. It may be noted that we have used the ratio of the magnetic moments for octahedral Mn^{4+} and trigonal prismatic Mn^{2+} of 2:1 for the present NPD pattern simulation. For these simulations we have also used the peak profile function yielded by Rietveld analysis at 298 K.

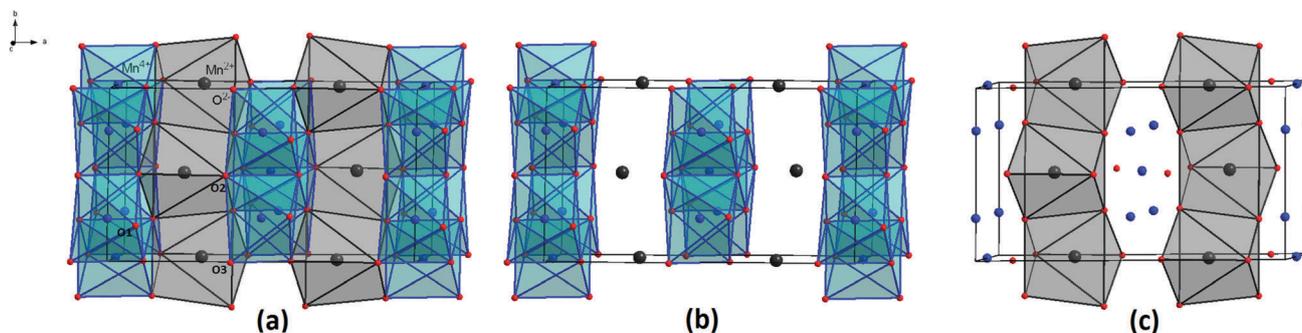As seen in Fig. 3, there is a magnetic contribution outside of the Bragg positions, *e.g.* (0 1 0) and (−1 0 1) arising from the

Fig. 1 (a) Polyhedral representation of Mn_5O_8 crystal structure, (b) octahedral coordination of Mn^{4+} atoms, and (c) trigonal prismatic coordination of Mn^{2+} atoms. The atom labels are given in (a).

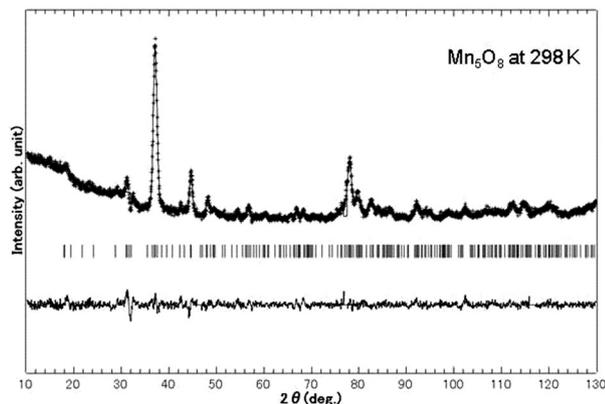This journal is © the Owner Societies 2016

Phys. Chem. Chem. Phys., 2016, **18**, 27885–27896 | 27887

Fig. 2 Experimental, calculated, and difference NPD patterns of Mn_5O_8 at 298 K. Bars denote Bragg positions; space group $C2/m$, $\lambda = 1.5556$ Å.
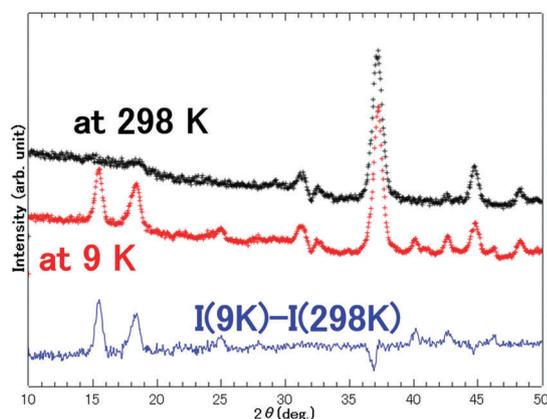

Fig. 3 Experimental NPD data at 298 K and 9 K, and the corresponding differential curve.

Fig. 4 The proposed magnetic structures M1, M2, M3, and M4 based on experimental measurements are shown as (a), (b), (c), and (d), respectively. The manganese ions with different spin moments are denoted as Mn1(red), Mn2(blue), and Mn3(grey) in these figures. The corresponding simulated Neutron Powder Diffraction patterns for Mn_5O_8 in these four magnetic models are given in the lower panel.

chemical unit cell with the space group $C2/m$ in the NPD pattern taken at 9 K. It is worth noting that there are no magnetic super reflections at (hkl) with non-integer value of h, k, and/or l, and hence one can rule out the possibility of forming complicated modulated magnetic ordering in Mn_5O_8. We have found that the magnetic model associated with M4 alone is compatible with the measured low temperature diffraction data with observed magnetic reflections. In this model, the magnetic moments at the Mn1, Mn2, and Mn3 (and symmetry related positions) sites exist only in the ac plane, and hence no magnetic component was found along the b-axis. The components of magnetic moment along a- and c-axes, $i.e.$ m_x and m_z, were refined using Rietveld refinement for Fig. 5 and those for Mn1, Mn2, and Mn3 sites are found to be 2.4 μ_B, 2.4 μ_B, and 3.8 μ_B, respectively. The refined magnetic moment data are tabulated in Table 1 for the 9 K NPD pattern.

Based on our experimental results we have proposed four different magnetic structure models for Mn_5O_8 namely M1, M2, M3, and M4 (see Fig. 4). So, in order to identify the ground state among these proposed four magnetic structures we have done ab $initio$ total energy calculation for all these four models by including spin–orbit coupling as well as Coulomb

Fig. 5 Experimental, calculated, and difference NPD patterns of Mn_5O_8 at 9 K. Upper and lower bars denote Bragg positions of nuclei and magnetic reflections, respectively. Space group $C2/m$, $\lambda = 1.5556$ Å.

correlation effects. Obviously, models M1 and M2 are similar in that Mn1 and Mn2 atoms are arranged FM in the layer, but coupled

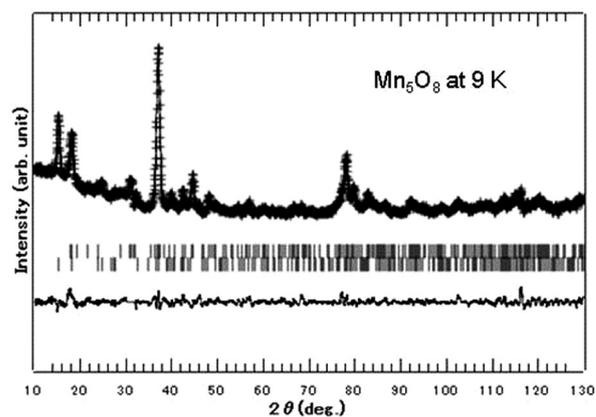**Table 1** The refined unit cell dimensions, atomic coordinates, and magnetic moments at various Mn sites for Mn_5O_8, derived from Rietveld refinement of NPD data 9 K well below the magnetic transition temperature are listed in this table. The crystal structure is found to be base centered monoclinic with space group $C2/m$. The calculated standard deviations are given in parentheses. $a = 10.325(2)$ Å, $b = 5.7181(7)$ Å, $c = 4.8594(6)$ Å, $\beta = 109.63(2)°$ $R_{wp} = 4.86\%$, $R_P = 3.67\%$, $\chi^2 = 2.08$

Atom								Moment[a]			
	Wyckoff position	x	y	z	Occupancy	B_{iso}[b] (Å^2)	M_x (μ_B)	M_y (μ_B)	M_z (μ_B)	M_{tot} (μ_B)
Mn1	2c (0 0 1/2)	0	0	1/2	1	0.2(2)	2.3(2)	0	1.8(2)	2.4(2)
Mn2	4g (0 y 0)	0	0.247(4)	0	1	0.2(2)	2.3(2)	0	1.8(2)	2.4(2)
Mn3	4i (x 0 z)	0.729(2)	0	0.665(5)	1	0.2(2)	4.02(9)	0	1.7(3)	3.8(2)
O1	8j (x y z)	0.114(2)	0.222(2)	0.395(2)	1	1.7(2)				
O2	4i (x 0 z)	0.114(2)	0	0.922(5)	1	1.7(2)				
O3	4i (x 0 z)	0.591(2)	0	0.872(4)	1	1.7(2)				

[a] Magnetic moments were constrained at same values for Mn1 and Mn2. [b] Isotropic atomic displacement parameters were constrained at same values for respectively, Mn and O.

AFM to the moments in the Mn3 layer, with moments aligned either perpendicular (M1) or parallel (M2) to the layers. These models give the overall ferrimagnetic structure. Models M3 and M4 are similar in the alignment of moments to models M2 and M1, respectively, but the orientation of the moments alternates as one goes from one Mn1/Mn2 layer to the next, and the moments in the Mn3 layer are coupled AFM, thus giving the overall AFM structure.

3.3 Electronic and magnetic properties

The input structural parameters used for the present calculations are taken from our NPD results obtained at 9 K (see Table 1). In order to identify the equilibrium structural parameters, we have performed the total energy calculation for Mn_5O_8 as a function of volume for the fully relaxed M4 structure as shown in Fig. 6. As the convergence is very slow due to the large number of atoms involved with spin polarization, spin orbit coupling, and Coulomb correlation effects included in the calculations, we have not done structural optimization for all the magnetic configurations discussed here, except for the ground state magnetic structure M4. Using a force minimization method in the Wien2k code, the atom positions are optimized. Moreover, in order to find the ground state with global minima we have adopted force as well as stress minimization methods implemented in VASP

code for the ground state magnetic configuration and the optimized structural parameters are compared with our NPD measurements. The calculated equilibrium structural parameters for Mn_5O_8 using VASP and Wien2k codes are compared with our low temperature NPD data in Table 3. The equilibrium volume obtained from Fig. 6 using the Birch–Murnaghan equation of states (EOS) is overestimated by only 1.1% compared with the experimental values and hence the calculated lattice parameters are in good agreement with the corresponding experimental values. From the EOS fit we have calculated the bulk modulus and its pressure derivative for Mn_5O_8, which are given in Table 3. Haines et al.[52] reported that the bulk modulus and its pressure derivative for β-MnO_2 are 3.28 Mbar and 4, respectively. The experimentally measured bulk modulus and its pressure derivative for MnO are 1.70 MBar and 4.8, respectively.[53] Using a linear muffin-tin orbital atomic sphere approximation (LMTO-ASA) approach, Cohen et al.[54] calculated the bulk modulus and its pressure derivative of MnO as 1.96 Mbar and 3.9, respectively. Our calculated bulk modulus for Mn_5O_8 is smaller than MnO and β-MnO_2. Hence, experimental high pressure studies are needed to confirm our predictions.

The calculated total density of states (DOS) for the proposed magnetic structures M1, M2, M3, and M4 are shown in Fig. 7. It may be noted that our GGA+SO calculations predict M1 magnetic configuration as ground state with ferrimagnetic half metallic behavior. A finite DOS is present in the minority-spin channel at E_F indicating metallic behavior. However, in the majority spin channel, a band gap of 1.283 eV opens up resulting in the half metallicity of the system. It may be noted that our GGA+SO calculations predict M1 magnetic configuration as the ground state with ferrimagnetic half metallic behavior. The calculated magnetic moments are listed in Table 4, which are in good agreement with the experimental neutron diffraction study. We found that the total DOS distribution and the spin moment
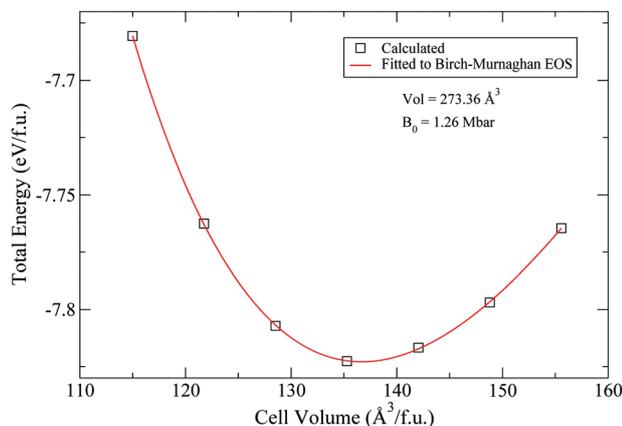
Fig. 6 Calculated total energy versus cell volume for Mn_5O_8 in the ground state M4 configuration.

Table 2 Calculated orbital magnetic moment (μ_B) at various Mn sites for Mn_5O_8 without (SO) and with orbital-polarization corrections (SO + OP)

	Orbital moment (Mn1/Mn2/Mn3)
M4 (SO)	−0.018/−0.023/0.006
M4 (SO + OP)	−0.022/−0.030/0.007

Paper

Table 3 Optimized structural parameters (a, b, c in Å, β in deg, equilibrium volume V_0 in Å^3), and bulk modulus (B_0 in Mbar) and its pressure derivative (B_0') for Mn_5O_8 in ground state M4 configuration from VASP and Wien2k^a calculations. Values given in parenthesis refer to the low temperature NPD measurements. The space group is $C2/m$ and $Z = 2$

Unit cell	Atom	Site	x	y	z	B_0	B_0'
$a = 10.3228(10.3250)$	Mn1	2c	0.0000(0.0000)	0.0000(0.0000)	0.5000(0.5000)	1.26	5.10
$b = 5.7436(5.7181)$			0.0000	0.0000	0.5000^a		
$c = 4.8887(4.8594)$	Mn2	4g	0.0000(0.0000)	0.2600(0.2470)	0.0000(0.0000)		
$\beta = 109.43(109.63)$			0.0000	0.2603	0.0000^a		
$V_0 = 273.36(270.24)$	Mn3	4i	0.7163(0.7290)	0.0000(0.0000)	0.6576(0.6550)		
			0.7173	0.0000	0.6595^a		
	O1	8j	0.1137(0.1140)	0.2272(0.2220)	0.3984(0.3950)		
			0.1134	0.2274	0.3995^a		
	O2	4i	0.1054(0.1140)	0.0000(0.0000)	0.9118(0.9220)		
			0.1049	0.0000	0.9119^a		
	O3	4i	0.6064(0.5910)	0.0000(0.0000)	0.9247(0.8720)		
			0.6062	0.0000	0.9252^a		

^{a} Optimised atom positions (x, y, z) calculated using the Wien2k code.
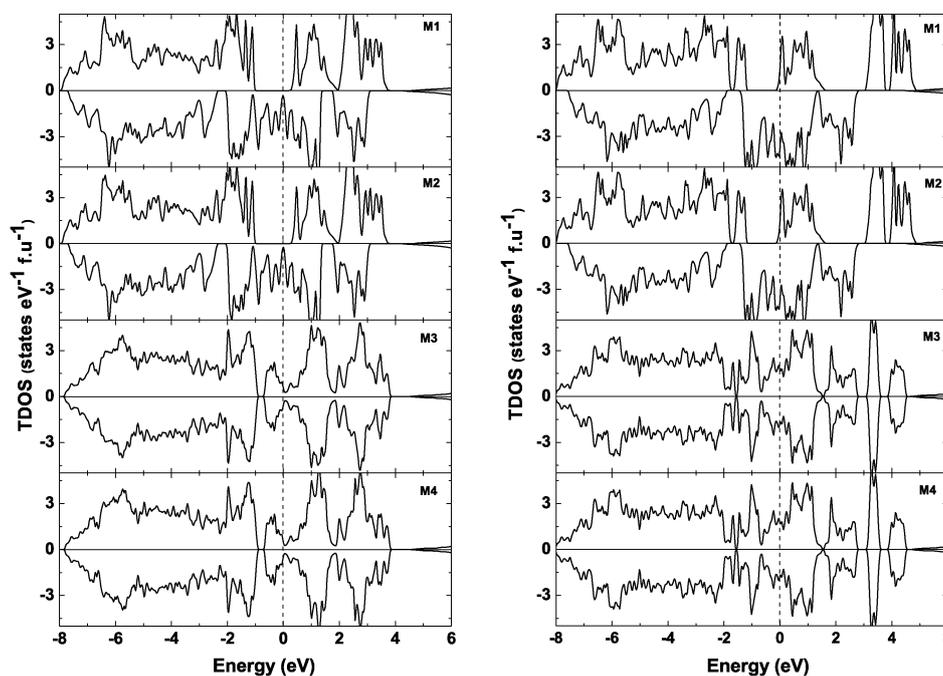
Fig. 7 The calculated total DOS for Mn_5O_8 in four different M1, M2, M3, and M4 magnetic configurations (described in the text). The DOS calculated using GGA+SO and GGA+SO+U are given in left and right panel, respectively. The Fermi level is set to zero.

are almost the same for M1 and M2; and also M3 and M4 which is consistent with our experimental observation. Even though our theoretical calculations predict the ferrimagnetic ground state, the experimentally observed magnetic structure corresponds to the antiferromagnetic state. So we concluded that GGA+SO calculations are unable to predict the correct magnetic ground state in Mn_5O_8.

It is well known that, the transition metal oxides usually have a strong Coulomb correlation which was not accounted for in the GGA+SO calculations. Hence, we have made total energy calculations by accounting Coulomb correlation effects through GGA+SO+U. Interestingly when we include the Coulomb correlation effect in our calculation, the total DOS obtained for M1 configuration having narrow d band states is moved towards

lower energy bringing metallic states instead of half metallic behavior. Furthermore, in a major spin channel we have found a sharp peak in the DOS curve indicating instability in the system. As a result, the M1 configuration becomes energetically unfavorable compared with the M4 configuration. In the case of M4 configuration, the magnetic moments are exactly canceled between various Mn sublattices bringing perfect antiferromagnetic ordering with metallic behavior, which is consistent with experimental observations. So, we can classify Mn_5O_8 as a strongly correlated antiferromagnetic metal. As the orbital moments obtained from relativistic spin-polarized calculations are usually smaller than the corresponding experimental value,[55] we have calculated the orbital moments (see Table 2) using orbital polarization correction proposed by Brooks and Eriksson et al.[56,57]

Table 4 The total magnetic moment, site projected magnetic moment at various Mn sites, and the relative total energy (ΔE) of various magnetic configurations with respect to the ground state are listed in this table

	Magnetic model	Total mom. (μ_B per f.u.)	Mn mom. Mn1/Mn2/Mn3 (μ_B per atom)	Total energy (meV per atom)
GGA+SO	M1	−0.99	2.26/2.30/−3.84	0
	M2	−0.99	2.26/2.30/−3.84	78.21
	M3	0	2.72/2.41/−3.83	52.32
	M4	0	2.72/2.41/−3.83	52.29
GGA+SO+U	M1	−1	2.51/2.59/−4.21	84.29
	M2	−1	2.51/2.59/−4.21	84.44
	M3	0	3.05/2.69/−4.18	0.04
	M4	0	3.05/2.69/−4.18	0
Exp.		0	2.4/2.4/−3.8	

We found that the calculated orbital moments obtained from SO calculation and SO + OP calculations are not changed much 0.0072 μ_B and also the estimated orbital moments are small 0.030 μ_B, as expected in transition metal compounds where spin–orbit coupling is generally weak.

The orbital-projected DOS for Mn 3d electrons in the ground state M4 magnetic configuration within GGA+SO+U is shown in Fig. 8. It is well known that the Mn d orbitals in octahedral coordination split into t_{2g} triplet (d_{xy}, d_{xz}, d_{yz}) and e_g doublet ($d_{x^2-y^2}$, d_{z^2}) by the cubic crystal field. As both Mn1 and Mn2 are in octahedral coordination with oxygen, their magnetic moments in these two sites can be analyzed easily using the orbital projected DOS. For Mn^{4+} oxidation state, there will be totally three d electrons which occupy the majority spin t_{2g} states and the e_g states will be empty in the high spin configuration. So one can expect 3 μ_B per Mn sites in a pure ionic picture. In conformity with the above view, our calculated DOS shows that the e_g states are almost empty in the valence band. Moreover, the t_{2g} states in the minority spin channel are negligibly small confirming the high-spin (HS) state of Mn^{4+} ions. However,
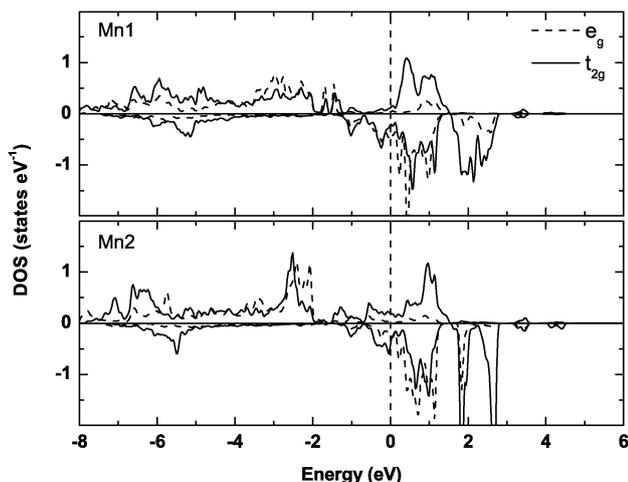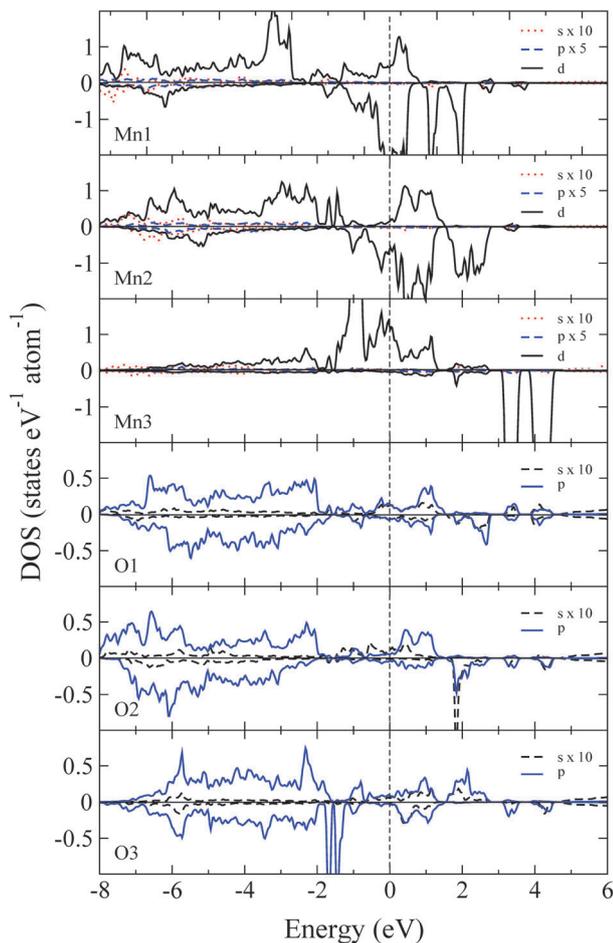

Fig. 8 The calculated orbital decomposed DOS for Mn1 and Mn2 sites of Mn$_5$O$_8$ in the ground state antiferromagnetic configuration obtained from GGA+SO+U. The Fermi level is set to zero.

the calculated magnetic moment (2.69 μ_B) in the Mn2 site is lower than 3 μ_B, indicating that there is a substantial covalent bond between Mn2–O. Usually, the electrons in solids may participate either in bonding or magnetism. Hence due to the covalency effect, the average bond length between Mn2–O(1.917 Å) is smaller than that between Mn1–O(1.926 Å). Owing to the short Mn2–O distance, there is a substantial induced moment of 0.027 μ_B per atom present in the oxygen sites around Mn2. However, the magnetic moment in oxygen sites around Mn1 is comparatively small 0.006 μ_B per atom. The calculated exchange splitting energy for Mn1 and Mn2 are 2.01 eV and 1.9 eV, respectively, correlating linearly with the corresponding magnetic moment. So, the larger exchange splitting at the Mn1 site could explain why Mn1 site has larger moments compared to the Mn2 site. Due to the Coulomb correlation effect d states get localized and hence the magnetic moment is increased in GGA+SO+U calculation as indicated in Table 4. As the pseudocubic crystal field operates in the MnO$_6$ octahedra, the electronic states at the Fermi level display both Mn(e_g) and Mn(t_{2g}) bands. The calculated energy difference between M3 and M4 models is less than 30 μeV only in the GGA+SO calculation and that is increased slightly to 40 μeV when we account correlation effect into the calculation. As mentioned above the GGA+SO+U calculation correctly predicted experimentally observed antiferromagnetic ground state with magnetic configuration of M4 suggesting the presence of a strong Coulomb correlation effect in this material.

The Mn d levels in a trigonal prismatic coordination split into non-degenerate 1a (d_{z^2}), doubly degenerate 1e (d_{xy},$d_{x^2-y^2}$), and doubly degenerate 2e (d_{xz},d_{yz}) levels. As there are five d electrons present in the Mn^{2+} ion residing in the Mn3 site, one would expect that these five electrons occupy the above mentioned levels. For the pure ionic case, the spin moment at the Mn3^t site in low-spin(LS; 1a^{2}1e^{3}2e^0), intermediate-spin (IS; 1a^{2}1e^{2}2e^1), and high-spin (HS; 1a^{1}1e^{2}2e^2) configurations will then be 1, 3, and 5 μ_B, respectively. The experimentally measured magnetic moment at the Mn3^t site is 3.8 μ_B, whereas our calculated magnetic moment gave a somewhat higher spin moment of 4.18 μ_B. The site-projected DOS for Mn and O atoms of Mn$_5$O$_8$ in the ground state M4 configuration are shown in Fig. 9. The bands originating from oxygen are lying in the energy range −8 and −2 eV which are almost completely filled. The DOS at E_F is mainly contributed by the Mn 3d states. From this figure, it is clear that the observed metallic behavior in Mn$_5$O$_8$ is mainly originating from Mn atoms with ∼18% contribution from oxygen. The minority spin electrons at the E_F for Mn3 are almost negligible indicating that the majority spin electrons alone participate in the electrical conductivity, as evident from the Fig. 9. We have observed a noticeable hybridization between the metal Mnd and the ligand Op states in the whole valence band indicating significant covalency in this system. As a result, the calculated magnetic moments in the Mn sites are smaller than those expected from a pure ionic picture. Owing to the covalency effect, the oxygen atoms close to Mn have non-negligible magnetic moments.

In order to understand the spin and valence states of Mn1^o, Mn2^o, and Mn3^t ions in Mn$_5$O$_8$ we have displayed the

Fig. 9 Calculated orbital-projected DOS for Mn and O sites of Mn_5O_8 in the ground-state M4 configuration obtained from GGA+SO+U. The Fermi level is set to zero. Note that s and p states of Mn and s states of O are magnified.

orbital-projected d-electron DOS of these Mn ions in Fig. 10. For d^3 system, Hund's rule predicts that the electrons will not pair and occupy the t_{2g} orbitals alone by leaving the e_g orbitals completely empty. As a result, Fig. 10 shows almost equal occupation of electrons in all the five d orbitals for $Mn1^o$ and $Mn2^o$. The electron occupation in the e_g orbitals of $Mn1^o$ and $Mn2^o$ bring strong covalent interaction between Mn^{4+} ions and oxygen in the whole valence band region. This figure reveals that $Mn3^t$ is in HS state as it is evident from the occupation of majority spin channel of all the five d orbitals. It is also clear that higher lying DOS of Mn3 (d_{yz} and d_{xz}) and O1 play an important role to bring metallic behavior in this compound.

It may be recalled that there are two types of exchange interactions one can expect between the magnetic cations in ionic crystals: cation–cation and cation–anion–cation (or even cation–anion–anion–cation) interactions. For the case of 90° cation–anion–cation interaction, Goodenough[58] has pointed out that if the octahedral interstices of two neighboring cations share a common edge then there is a direct overlap of the d_{xy} or d_{yz} or d_{xz} orbitals of these two cations. As a result, the anion plays a less obvious role in the delocalization–superexchange process.

In Mn_5O_8 also the Mn ions $Mn1^o$, $Mn2^o$ form edge-shared octahedra and hence the interaction between the two neighboring Mn ions can be referred to as cation–cation interactions. When the cation–cation separation is short and the t_{2g} orbitals are half filled, then cation–cation interactions tend to dominate the 90° superexchange. In the present case also the interatomic distance between Mn1 and Mn2 is small (2.81 Å) and comparable to other magnetic oxides such as $NaCrO_2$ (2.96 Å) and $NaFeO_2$ (3.02 Å).[59] It is expected that in the octahedral crystal field the Mn^{4+} ions in the HS state will have a half filled t_{2g} level as we have seen in the orbital decomposed DOS analysis (see Fig. 10). It was also emphasized by Kanamori[60] that, the exchange interaction J_{ij}^{c-c} for the two half filled orbitals expected to be negative results in antiferromagnetic interaction. In consistence, the Mn^{4+} ions in Mn_5O_8 share edges with each other and hence the 90° superexchange interactions are responsible for the observed antiferromagnetic ordering. It may be noted that our experimentally measured Weiss constant θ value for Mn_5O_8 is -144.5 K[28] which further reiterates the antiferromagnetic superexchange interactions as mentioned above.

When we analyze orbital decomposed DOS for the oxygen p states, no noticeable p_z states are present between -2 eV to 0 eV (E_F). On the other hand, the orbital decomposed DOS for the d states of Mn3 ion shows that the majority of d states are present in this energy range. Hence, super-exchange path way is not possible between oxygen p_z states and Mn3 d states, as evident from Fig. 10 and angular momentum projected DOS (Fig. S1, ESI†). This could explain why the intralayer coupling between Mn atoms is of ferromagnetic in nature.

Mn1 and Mn2 d states are spread in the whole valence band from -8 eV to E_F with dominant contributions from d_{xy} and d_{xz} states near the E_F. The DOS analysis of Mn1 and Mn2 sites shows strong distribution in the energy range -4 eV to -2 eV in the valence band. Moreover, the orbital decomposed DOS for oxygen p states show that both p_x and p_y states are present in this energy range. Hence there is a possibility of superexchange antiferromagnetic interaction between oxygen p_x and p_y states with Mn1/Mn2 d states between the layer. As a result, one could expect AFM interaction between the layers and FM interaction within the layer leading to A-AFM ordering. Consistent with the conclusion arrived from DOS analysis, our total energy calculations also show that the A-AFM ordering is the lowest energy configuration in this system. The theoretical finding of A-AFM ordering in Mn_5O_8 could also support the experimentally observed negative Curie temperature value from the susceptibility measurements.[28]

3.4 Bonding analysis through COHP

The crystal orbital Hamiltonian population (COHP) is calculated using VASP to analyze the bond strength and character of the bonding interactions between the constituents in Mn_5O_8.[61,62] COHP is constructed by weighing the DOS with the corresponding Hamiltonian matrix.[63] This approach provides a qualitative description of the bonding (negative COHP) and antibonding (positive COHP) interactions between atoms. Fig. 11 displays the calculated COHP for the Mn1–O1, Mn1–O2, Mn2–O1, Mn2–O2,
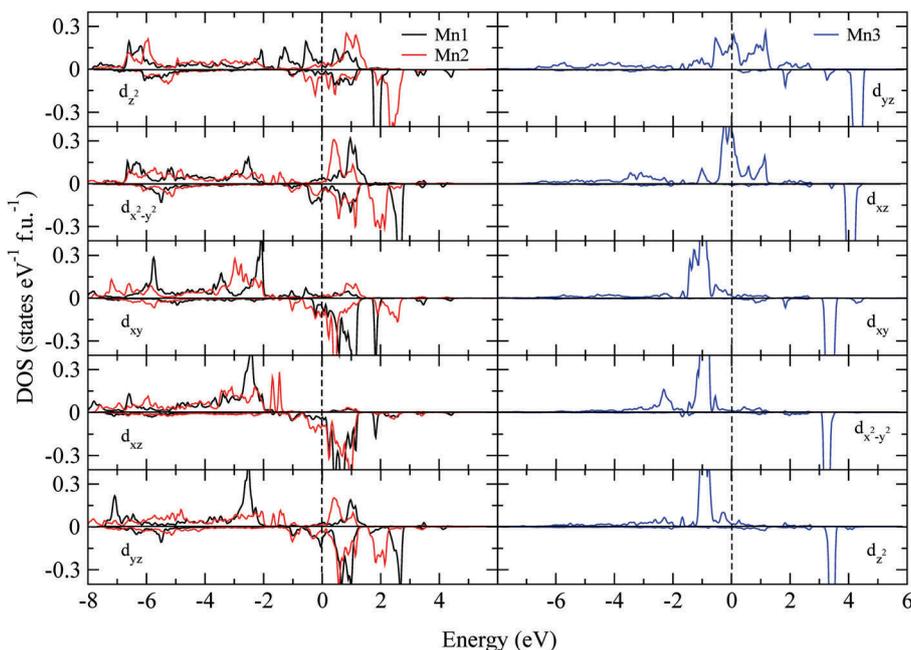
27892 | *Phys. Chem. Chem. Phys.,* 2016, **18**, 27885–27896

This journal is © the Owner Societies 2016

Fig. 10 Orbital (d) decomposed DOS for $Mn1^o$, $Mn2^o$ and $Mn3^t$ in Mn_5O_8 for the ground-state M4 configuration. The Fermi level is set to zero.
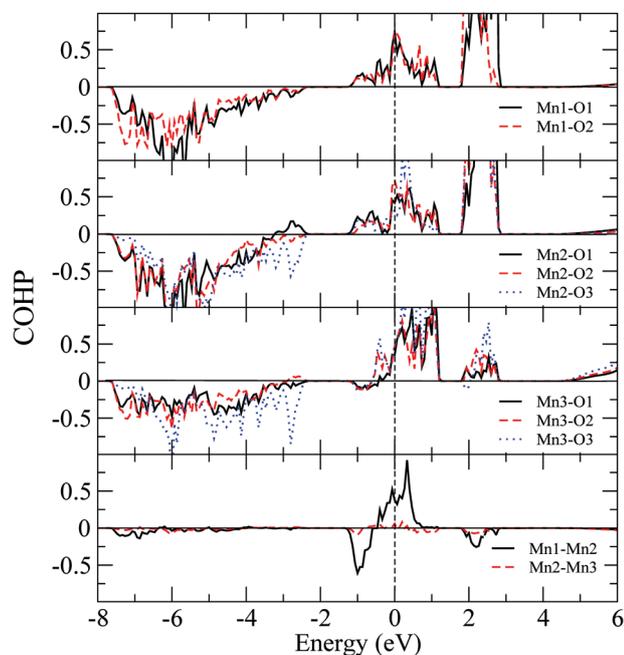

Fig. 11 The calculated COHP for Mn1–O1, Mn1–O2, Mn2–O1, Mn2–O2, Mn2–O3, Mn3–O1, Mn3–O2, Mn3–O3, Mn1–Mn2 and Mn2–Mn3 in ground-state M4 configuration of Mn_5O_8.

Mn2–O3, Mn3–O1, Mn3–O2, Mn3–O3, Mn1–Mn2, and Mn2–Mn3 interactions in Mn_5O_8. The COHP curves reveal that the Mn–O bonding states are present strongly in the region −7.5 to −2.3 eV of the valence band. In the vicinity of the E_F (i.e., within −1 eV to E_F) in Mn–O COHP noticeable antibonding states are present. As the Mn–Mn interactions were screened by oxygen ions present between the Mn ions, the calculated Mn–Mn bonding

states distribution is relatively small. We have calculated the bond strength between various constituents of Mn_5O_8 using the Integrated COHP (ICOHP) as we have done earlier.[48] The calculated ICOHP for various constituents of Mn_5O_8 reflecting the bond strength between the atoms are listed in Table 5. According to Table 5, Mn–O has the strongest bonding interaction in Mn_5O_8. The bonding interaction between Mn2–Mn3 is very weak since the bond distance between these atoms is relatively high (~ 3 Å). The MnO_6 octahedra are highly distorted and hence the Mn2–O distances vary between 1.890 Å to 1.955 Å and correspondingly the calculated bond strength varies from −2.17 eV to −2.33 eV. The calculated bond length for $Mn1–O_a$ is 1.993 Å and that for $Mn2–O_a$ is 1.938 Å where, O_a is apical oxygen in the octahedra. Hence, one can expect that the $Mn2–O_a$ bond will have a stronger bond strength than $Mn1–O_a$. In agreement, our calculated ICOHP value for $Mn2–O3_a$ is larger than that for $Mn1–O2_a$. If there are strong bonds present between magnetic cations with anions, one can expect that the magnetic moment will quench. The calculated bond strength between constituents obtained based on ICOHP values listed in Table 5

Table 5 Calculated bond strength from Integrated COHP

Interaction	Bond strength (eV)
Mn1–O1	−2.18
Mn1–O2	−1.84
Mn2–O1	−2.27
Mn2–O2	−2.17
Mn2–O3	−2.33
Mn3–O1	−1.35
Mn3–O2	−1.27
Mn3–O3	−2.04
Mn1–Mn2	−0.26
Mn2–Mn3	−0.05

Table 6 Selected inter-atomic distances (Å) and bond valence sum (BVS) for Mn_5O_8 at 9 K. Calculated standard deviations are listed in parentheses

	Mn1	Mn2	Mn3
O1	1.91(2) × 4	1.89(2) × 2	2.15(2) × 4
O2	1.99(2) × 2	1.96(2) × 2	2.10(3)
O3		1.94(2) × 2	2.00(3)
BVS	3.7(2)	3.7(2)	2.3(2)

Note: BVS values were calculated by iteration from initial arbitrary mixed-valence value. The bond valence parameter was assumed by taking fraction of standard literature values; Mn^{2+}–O^{2-}, Mn^{3+}–O^{2-}, and Mn^{4+}–O^{2-} are 1.79, 1.76, and 1.753 respectively.

are reflecting the variation in magnetic moments in the corresponding Mn atoms (see Table 4). Moreover the difference in the average bond strength for Mn1–O and Mn2–O indicates that the Mn atoms in Mn_5O_8 are in two different oxidation states, consistent with our DOS analysis.

The formal oxidation states of the octahedral and trigonal-prismatic Mn atoms can be evaluated from bond-valence-sum (BVS) calculations, by using bond-valence parameters of $R_{ij}(Mn^{2+}) = 1.79$, $R_{ij}(Mn^{3+}) = 1.76$ and $R_{ij}(Mn^{4+}) = 1.753$, and bond distances of d_{ij}, yielded from NPD analysis at 9 K, in the formula $\Sigma \exp[(R_{ij} - d_{ij})/0.37]$. The results indicate that octahedral coordinated Mn atoms at 2c (Mn1) and 4g (Mn2) sites are tetravalent and trigonal-prismatic coordinated Mn atom at 4i (Mn3) site is divalent (see Table 6), even though the BVS values for octahedral and trigonal-prismatic polyhedral deviate slightly from the ideal value of 3.7(2) and 2.3(2), respectively.

The valence states of Mn in Mn_5O_8 can be written as $Mn_2^{2+}Mn_3^{4+}O_8$, the spin-only magnetic moment for Mn_5O_8 can be calculated from the expression

$$\mu_{\text{eff}} = \sqrt{\frac{2}{5}\left[\mu_{\text{Mn(II)}}\right]^2 + \frac{3}{5}\left[\mu_{\text{Mn(IV)}}\right]^2} \quad (1)$$

An effective magnetic moment measured from magnetic susceptibility study is $\mu_{\text{eff}} = 4.803 \ \mu_B$. The calculated effective magnetic moment using $\mu_{\text{Mn(II)}} = 5.9 \ \mu_B$ and $\mu_{\text{Mn(IV)}} = 3.87 \ \mu_B$ is $\mu_{\text{eff}} = 4.786 \ \mu_B$. The close agreement between the calculated spin-only magnetic moment and the experimental moment confirms the presence of mixed valence states in Mn_5O_8. As the experimentally measured effective magnetic moment is close to the theoretically calculated spin-only value, it is apparent that the orbital angular moment is quenched due to the ligand field splitting. This is also evident from Table 2 showing that our calculated orbital moment is very small and the spin moment mainly contributes to the total magnetic moment.

In previous study,[28] we have mentioned the possibility of Mn_3O_4[64] as secondary phase in master Mn_5O_8 sample, based on the observed magnetic ferroic transition around 40 K. In present study, we have measured NPD at 70 (Fig. S2, ESI†) i.e. above 40 K but still below $T_N = 133$ K. However, no unique change is noticeable compared to the NPD data at 9 K. Therefore, we conclude that there is no major contribution from the secondary phase of Mn_3O_4 in the collected NPD data.

4 Conclusions

To summarize, magnetic ordering and the mixed valent nature of Mn_5O_8 have been reported using fully relativistic density functional theory calculations and Neutron powder diffraction measurements. From our total energy calculation we have predicted that Mn_5O_8 orders antiferromagnetically with the spin orientation along [100] direction in accordance with our NPD measurements. Among the four different magnetic models proposed from the experiments, M4 magnetic configuration is found to be the ground state magnetic structure in Mn_5O_8. Density of states analysis shows a large DOS at E_F in the ground state magnetic structure showing the metallic nature of Mn_5O_8. Calculations without the inclusion of Hubbard U leads to ferrimagnetic half metallic state as ground state, contradictory to the experimental findings, indicating the presence of strong Coulomb correlation effect in this material. However, by including Coulomb correlation effect in to the calculations we could correctly predict the ground state as antiferromagnetic metal. Presence of two different magnetic moments along with the different density of states distribution in the Mn sites illustrate the mixed valent behavior of Mn ions. Bond strength analysis based on COHP between constituents indicates strong anisotropy in the bonding behavior which results from layered nature of the crystal structure. The orbital decomposed DOS analysis of Mn d states shows that Mn ions in the Mn^{4+} and Mn^{2+} oxidation states with high spin magnetic configuration. Our bond valence sum analysis also supports the presence of two different oxidation states such as 4+ and 2+ in this compound. The calculated orbital moment using relativistic spin polarized calculation with orbital polarization correction yielded very small orbital moment and hence the spin-only moment is sufficient to account for the experimentally measured effective moment from susceptibility measurements. The over all results indicate that Mn_5O_8 can be described as a strongly correlated mixed valent antiferromagnetic metal.

Appendix: group theory analysis for Mn_5O_8

To determine magnetic structure of Mn_5O_8, the possible magnetic structures, which are compatible with the crystal symmetry, were investigated by the method described by Bertaut.[65] The magnetic structures are defined by the basis vectors of the irreducible representations of the little group Γ_k which for a propagation vector $k = (-1, 0, 1)$ coincides with the crystallographic space group.

In the case of Mn_5O_8 the Mn atoms are in wyckoff sites at 2c, 4g, and 4i under space group of $C2/m$. The decomposition of the representation Γ, describing the transformation properties of the magnetic moments is given by $\Gamma = \Gamma_1 + 2\Gamma_3$ in Kovalev's notation.[66] The solutions defined by Γ_1 correspond to FM ordering within layers and AFM ordering between each layer with magnetic moments parallel to the b direction (M3 in Fig. 4). Γ_5 defines similar ordering with F1 in the ac plane (M4 in Fig. 4).

References

1 J. Van Elp, R. Potze, H. Eskes, R. Berger and G. Sawatzky, *Phys. Rev. B: Condens. Matter Mater. Phys.*, 1991, **44**, 1530.

2 S. Geller, *Acta Crystallogr., Sect. B: Struct. Crystallogr. Cryst. Chem.*, 1971, **27**, 821–828.

3 T. Gao, H. Fjellvåg and P. Norby, *Anal. Chim. Acta*, 2009, **648**, 235–239.

4 C. Franchini, R. Podloucky, J. Paier, M. Marsman and G. Kresse, *Phys. Rev. B: Condens. Matter Mater. Phys.*, 2007, **75**, 195128.

5 P. Ravindran, A. Kjekshus, H. Fjellvåg, A. Delin and O. Eriksson, *Phys. Rev. B: Condens. Matter Mater. Phys.*, 2002, **65**, 064445.

6 R. D. Shannon, *Acta Crystallogr., Sect. A: Cryst. Phys., Diffr., Theor. Gen. Crystallogr.*, 1976, **32**, 751–767.

7 M. M. Thackeray, *Prog. Solid State Chem.*, 1997, **25**, 1–71.

8 J. E. Post, *Proc. Natl. Acad. Sci. U. S. A.*, 1999, **96**, 3447–3454.

9 R. Vidya, P. Ravindran, P. Vajeeston, A. Kjekshus and H. Fjellvåg, *Phys. Rev. B: Condens. Matter Mater. Phys.*, 2004, **69**, 092405.

10 R. Vidya, P. Ravindran, A. Kjekshus and H. Fjellvåg, *Phys. Rev. B: Condens. Matter Mater. Phys.*, 2002, **65**, 144422.

11 C. Franchini, V. Bayer, R. Podloucky, J. Paier and G. Kresse, *Phys. Rev. B: Condens. Matter Mater. Phys.*, 2005, **72**, 045132.

12 M. Imada, A. Fujimori and Y. Tokura, *Rev. Mod. Phys.*, 1998, **70**, 1039.

13 N. Mott, *Rev. Mod. Phys.*, 1968, **40**, 677.

14 W. A. Harrison, *Phys. Rev. B: Condens. Matter Mater. Phys.*, 2008, **77**, 245103.

15 H. Shaked, J. Faber Jr and R. Hitterman, *Phys. Rev. B: Condens. Matter Mater. Phys.*, 1988, **38**, 11901.

16 K. Dwight and N. Menyuk, *Phys. Rev. B: Condens. Matter Mater. Phys.*, 1960, **199**, 1470.

17 G. Jensen and O. Nielsen, *J. Phys. C: Solid State Phys.*, 1974, **7**, 409.

18 G. Srinivasan and M. S. Seehra, *Phys. Rev. B: Condens. Matter Mater. Phys.*, 1983, **28**, 1.

19 A. Yoshimori, *J. Phys. Soc. Jpn.*, 1959, **14**, 807–821.

20 H. Sato, K. Wakiya, T. Enoki, T. Kiyama, Y. Wakabayashi, H. Nakao and Y. Murakami, *J. Phys. Soc. Jpn.*, 2001, **70**, 37–40.

21 M. Sugawara, M. Ohno and K. Matsuki, *Chem. Lett.*, 1991, 1465–1468.

22 C. Azzoni, M. Mozzati, P. Galinetto, A. Paleari, V. Massarotti, D. Capsoni and M. Bini, *Solid State Commun.*, 1999, **112**, 375–378.

23 J. H. Rask and P. R. Buseck, *Am. Mineral.*, 1986, **71**, 805–814.

24 G. B. Ansell, M. A. Modrick, J. Longo, K. Poeppeimeler and H. Horowitz, *Acta Crystallogr., Sect. B: Struct. Crystallogr. Cryst. Chem.*, 1982, **38**, 1795–1797.

25 A. Riou and A. Lecerf, *Acta Crystallogr., Sect. B: Struct. Crystallogr. Cryst. Chem.*, 1977, **33**, 1896.

26 N. Yamamoto, M. Kiyama and T. Takada, *J. Appl. Phys.*, 1973, **12**, 1827.

27 A. Punnoose, H. Magnone and M. Seehra, *IEEE Trans. Magn.*, 2001, **37**, 2150–2152.

28 T. Gao, P. Norby, F. Krumeich, H. Okamoto, R. Nesper and H. Fjellvåg, *J. Phys. Chem. C*, 2010, **114**, 922–928.

29 S. Thota, B. Prasad and J. Kumar, *Mater. Sci. Eng., B*, 2010, **167**, 153–160.

30 I. Uddin, P. Poddar and A. Ahmad, *J. Nanoeng. Nanomanuf.*, 2013, **3**, 91–97.

31 X. Zheng, C. Xu, K. Nishikubo, K. Nishiyama, W. Higemoto, W. Moon, E. Tanaka and E. S. Otabe, *Phys. Rev. B: Condens. Matter Mater. Phys.*, 2005, **72**, 014464.

32 L. He, C. Chen, N. Wang, W. Zhou and L. Guo, *J. Appl. Phys.*, 2007, **102**, 103911.

33 Y.-F. Han, F. Chen, Z. Zhong, K. Ramesh, L. Chen and E. Widjaja, *J. Phys. Chem. B*, 2006, **110**, 24450–24456.

34 D. Jeong, K. Jin, S. E. Jerng, H. Seo, D. Kim, S. H. Nahm, S. H. Kim and K. T. Nam, *ACS Catal.*, 2015, **5**, 4624–4628.

35 R. Vidya, P. Ravindran, H. Fjellvåg and A. Kjekshus, *Phys. Rev. B: Condens. Matter Mater. Phys.*, 2006, **74**, 054422.

36 T. Gao, F. Krumeich, R. Nesper, H. Fjellvåg and P. Norby, *Inorg. Chem.*, 2009, **48**, 6242–6250.

37 B. C. Hauback, H. Fjellvåg, O. Steinsvoll, K. Johansson, O. T. Buset and J. Jørgensen, *J. Neutron Res.*, 2000, **8**, 215.

38 H. Rietveld, *J. Appl. Crystallogr.*, 1969, **2**, 65–71.

39 J. Rodríguez-Carvajal, *Physica B*, 1993, **192**, 55–69.

40 P. Blaha, K. Schwarz, G. Madsen, D. Kvasnicka and J. Luitz, *An augmented plane wave + local orbitals program for calculating crystal properties*, 2001.

41 J. Perdew, K. Burke and M. Ernzerhof, *Phys. Rev. Lett.*, 1996, **78**, 1396.

42 M. Cococcioni and S. De Gironcoli, *Phys. Rev. B: Condens. Matter Mater. Phys.*, 2005, **71**, 035105.

43 V. Anisimov and O. Gunnarsson, *Phys. Rev. B: Condens. Matter Mater. Phys.*, 1991, **43**, 7570.

44 V. I. Anisimov, J. Zaanen and O. K. Andersen, *Phys. Rev. B: Condens. Matter Mater. Phys.*, 1991, **44**, 943.

45 V. I. Anisimov, I. Solovyev, M. Korotin, M. Czyżyk and G. Sawatzky, *Phys. Rev. B: Condens. Matter Mater. Phys.*, 1993, **48**, 16929.

46 A. Liechtenstein, V. Anisimov and J. Zaanen, *Phys. Rev. B: Condens. Matter Mater. Phys.*, 1995, **52**, R5467.

47 G. Kresse and J. Furthmüller, *Comput. Mater. Sci.*, 1996, **6**, 15–50.

48 P. Ravindran, R. Vidya, A. Kjekshus, H. Fjellvåg and O. Eriksson, *Phys. Rev. B: Condens. Matter Mater. Phys.*, 2006, **74**, 224412.

49 S. M. Auerbach, K. A. Carrado and P. K. Dutta, *Handbook of Layered Materials*, Marcel Dekker, Inc., New York, 2004, pp. 475–508.

50 H. R. Oswald and M. J. Wampetich, *Helv. Chim. Acta*, 1967, **50**, 2023.

51 H. Oswald, W. Feitknecht and M. Wampetich, *Nature*, 1965, **207**, 72.

52 J. Haines, J. M. Leger and S. Hoyau, *J. Phys. Chem. Solids*, 1995, **56**, 965–973.

53 R. Jeanloz and A. Rudy, *J. Geophys. Res.: Solid Earth*, 1987, **92**, 11433–11436.

54 R. E. Cohen, I. Mazin and D. G. Isaak, *Science*, 1997, **275**, 654–657.

55 P. Ravindran, A. Kjekshus, H. Fjellvåg, P. James, L. Nordström, B. Johansson and O. Eriksson, *Phys. Rev. B: Condens. Matter Mater. Phys.*, 2001, **63**, 144409.

56 M. Brooks, *Physica B*, 1985, **130**, 6–12.

57 O. Eriksson, B. Johansson and M. Brooks, *J. Phys.: Condens. Matter*, 1989, **1**, 4005.

58 J. Goodenough, *Magnetism and the Chemical Bond*, Wiley, New York, 1963.

59 K. Motida and S. Miyahara, *J. Phys. Soc. Jpn.*, 1970, **28**, 1188–1196.

60 J. Kanamori, *J. Phys. Chem. Solids*, 1959, **10**, 87–98.

61 V. L. Deringer, A. L. Tchougréeff and R. Dronskowski, *J. Phys. Chem. A*, 2011, **115**, 5461–5466.

62 S. Maintz, V. L. Deringer, A. L. Tchougréeff and R. Dronskowski, *J. Comput. Chem.*, 2013, **34**, 2557–2567.

63 R. Dronskowski and P. E. Bloechl, *J. Phys. Chem.*, 1993, **97**, 8617–8624.

64 W. S. Seo, H. H. Jo, K. Lee, B. Kim, S. J. Oh and J. T. Park, *Angew. Chem., Int. Ed.*, 2004, **43**, 1115–1117.

65 E. Bertaut, *Acta Crystallogr., Sect. A: Cryst. Phys., Diffr., Theor. Gen. Crystallogr.*, 1968, **24**, 217–231.

66 O. V. Kovalev, *Irreducible representations of the space groups*, Gordon and Breach, New York, 1985.